Research Square

Preprints are preliminary reports that have not undergone peer review.
They should not be considered conclusive, used to inform clinical practice,
or referenced by the media as validated information.

Cotton-straw-derived sulfonated lignin/bentonite composites: Preparation and methylene blue adsorption performance

Nuermaimaiti Yimamu
Xinjiang University
Zheng Zheng Yao
Xinjiang University
Xin Yu Wu
Xinjiang University
Kai Ze Ding
Xinjiang University
Tursunjan Aydan
tursun714@xju.edu.cn
Xinjiang University

Research Article

Keywords: Lignin extraction, Sulfonated lignin-bentonite composites, Methylene blue, Adsorption

Posted Date: November 9th, 2026

DOI: https://doi.org/10.21203/rs.3.rs-11083850/v1

License: This work is licensed under a Creative Commons Attribution 4.0 International License.
Read Full License

Additional Declarations: No competing interests reported.

Cotton-straw-derived sulfonated lignin/bentonite composites: Preparation and methylene blue adsorption performance

Nuermaimaiti Yimamu[1,a], *Zheng Zheng Yao*[1,a], *Xin Yu Wu*[a], *Kai Ze Ding*[a], *Tursunjan Aydan*[*,a]

*a.*Key Laboratory of Oil and Gas Fine Chemicals, Ministry of Education & Xinjiang Uygur Autonomous Region, School of Chemical Engineering, Xinjiang University, Urumqi, 830017, China.

Abstract

Cotton straw is an abundant lignocellulose-rich agricultural residue that provides a sustainable and low-cost source of lignin. In this study, lignin was first extracted from cotton straw using a lactic acid-based deep eutectic solvent and then sulfonated to prepare two lignin/bentonite composites—LS/B (raw bentonite) and LS/CB (calcined bentonite)—as functional adsorbents. The composites were systematically characterized for their physicochemical properties, and their adsorption performance toward methylene blue (MB) was evaluated. Under optimized conditions, LS/B and LS/CB delivered remarkable MB adsorption capacities of 238.61 and 277.56 $mg \cdot g^{-1}$, respectively. The adsorption data fitted well to the pseudo-second-order kinetic and Langmuir isotherm models, indicative of monolayer chemisorption. Thermodynamic parameters confirmed the spontaneous and endothermic nature of the adsorption process. Mechanistically, adsorption was predominantly governed by electrostatic interactions, with synergistic contributions from π–π stacking and hydrogen bonding. Notably, LS/CB exhibited favorable recyclability, retaining 71.41% of its initial removal efficiency (86.37%) after five consecutive adsorption–desorption cycles. These findings demonstrate the valorization of cotton straw waste into efficient

[1] These authors contributed equally to this work.

* Corresponding author: Tursunjan Aydan； Email address: tursun714@xju.edu.cn

adsorbents for dye wastewater treatment, offering a scalable strategy applicable to other lignin-rich biowastes including agricultural waste and black liquor.

Key words: Lignin extraction; Sulfonated lignin-bentonite composites; Methylene blue; Adsorption

1 Introduction

Cotton straw is a lignocellulose-rich agricultural residue, with lignin constituting 15-30 wt% of its biomass [1,2]. As a major component of plant cell walls, lignin is a natural aromatic polymer containing phenolic hydroxyl, methoxyl, and carboxyl groups [3,4]. These functionalities confer inherent adsorption activity, making lignin a promising low-cost precursor for functional materials [5]. However, conventional lignin extraction methods typically employ harsh alkaline or organic solvents, which are energy-intensive and environmentally unfavorable [6,7]. Deep eutectic solvents (DES) have therefore emerged as an attractive alternative for lignin isolation due to their low cost, easy preparation, and mild operating conditions [8].

Despite its innate active groups, native lignin suffers from a complex and heterogeneous structure that leads to limited chemical reactivity, restricting its direct utilization in high-value applications [9,10]. Various modification strategies—including sulfonation, amination, phenolation, and graft copolymerization—have been developed to tailor its structure and enhance compatibility and reactivity [11,12]. These approaches introduce additional functional groups and increase the accessibility of inherent ones, thereby significantly strengthening lignin's ability to adsorb organic dyes and heavy metal ions through hydrogen bonding, electrostatic interaction, and complexation [13], related lignin-based materials have been extensively reported [14-16].

Nevertheless, lignin molecules tend to aggregate due to strong intermolecular hydrogen bonding and π–π stacking, which reduces active site accessibility [17]. The limited active sites and steric hindrance of lignin hinder the formation of mechanically robust hydrogel networks [18]. To address these issues, organic–inorganic composite hydrogels have attracted considerable attention. Such systems integrate the adsorption functionality of biomass polymers with the structural stability of mineral phases[19], serving as low-cost, renewable alternatives to activated carbon, whose high cost and poor regeneration hinder large-scale application .

In recent years, lignin/bentonite composite adsorbents have attracted increasing attention. Bentonite, a naturally abundant layered aluminosilicate, possesses high cation-exchange capacity and expandable interlayer spaces, making it an ideal candidate for constructing lignin-based composites [20,21]. Fu et al.[22] intercalated quaternized lignin into bentonite interlayers, increasing the specific surface area from 16.43 to 45.60 m^2/g and achieving a methylene blue adsorption capacity of 822.22 $mg \cdot g^{-1}$. Fang et al.[23] incorporated amino-functionalized montmorillonite nanosheets into a lignin/poly(vinyl alcohol) matrix via glutaraldehyde crosslinking, achieving a Pb(II) adsorption capacity of 190.22 $mg \cdot g^{-1}$. Our previous quaternary ammonium lignin/CTAB-modified bentonite hydrogel (LT/BC) achieved a methylene blue capacity of 151.20 $mg \cdot g^{-1}$, yet its efficiency dropped sharply from 94.14% to 61.41% after merely four cycles due to the poor water solubility of unmodified lignin and weak interfacial binding [24]. To address this, the present work employs sulfonated DES lignin and calcined bentonite to enhance interfacial compatibility and structural stability, aiming to construct composite hydrogels with superior adsorption capacity and cycling durability.

In this study, cotton straw-derived lignin was hydroxymethylated with

formaldehyde prior to sulfonation with sodium sulfite (Na_2SO_3). Two novel composite hydrogels with three-dimensional network structures were then fabricated by graft copolymerization of the LS with bentonite or CB, using acrylamide (AM) as the monomer, ammonium persulfate (APS) as the initiator, and N,N'-methylenebisacrylamide (MBA) as the cross-linker. The structural, compositional, surface, and morphological characteristics of the materials were comprehensively characterized using FT-IR, XRD, TG-DTG, SEM, and XPS. Furthermore, adsorption isotherm, kinetic, and thermodynamic models were established to elucidate the MB adsorption mechanism, and the regeneration performance of the materials was evaluated. This work aims to provide experimental insights into the fabrication strategies and structure-activity relationships of lignin-bentonite-based composite hydrogels.

2 Materials and Methods

2.1 Materials

All chemicals were of analytical grade and used as received. Acrylamide (AM, >98%), *N,N′*-methylenebisacrylamide (MBA, AR), (B, AR), and choline chloride (ChCl, AR) were bought from Shanghai Macklin Biochemical Technology Co., Ltd. (Shanghai, China). Tianjin Xin Bote Chemical Co., Ltd. (Tianjin, China) supplied methylene blue (MB, AR), sodium hydroxide (NaOH, AR), lactic acid (LA, AR), anhydrous ethanol (C_2H_5OH, AR), ethylene glycol (EG, AR), and oxalic acid (OA, AR). Ammonium persulfate (APS, >98%) and acetic acid (AA, AR) were products of Tianjin Zhiyuan Chemical Reagent Co., Ltd. (Tianjin, China). For pH adjustment and lignin content determination, hydrochloric acid (HCl, AR) and sulfuric acid (H_2SO_4, >98%) were acquired from Xilong Scientific Co., Ltd. (Sichuan, China). Sodium sulfite (Na_2SO_3, >99.5%) was procured from Xi'an Chemical Reagent Factory (Xi'an, China),

and commercial lignin (>98%) from Shanghai Aladdin Biochemical Technology Co., Ltd. (Shanghai, China). Deionized water was prepared in the laboratory. Raw bentonite was calcined in a muffle furnace at 550 °C for 2 h to yield calcined bentonite (CB), which was then sealed and stored at room temperature.

2.2 Preparation of LA-lignin

Lignin was extracted from cotton straw using a choline chloride/lactic acid deep eutectic solvent (DES). The extraction parameters, including DES type, temperature, time, molar ratio, solid-to-liquid ratio, and ultrasonication time, were optimized as detailed in Section 3.1. The as-prepared lignin denoted as LA-Lignin, dealkalized lignin and the solid residue were characterized by FTIR, XRD, TG/DTG, and SEM to confirm their structural features and thermal stability (Supplementary Information, Section 2, Fig. S1 and Fig. S2).

2.3 Determination of Lignin content

Lignin content was determined using the National Renewable Energy Laboratory (NREL) protocol [25]. Accurately weighed cotton straw samples (300.0 ± 3.0 mg) were mixed with 72% H_2SO_4 (3.00 ± 0.01 mL) and subjected to concentrated acid hydrolysis in a water bath at 30 ± 3 °C for 60 min. Subsequently, deionized water (84.00 ± 0.04 mL) was added to dilute the acid concentration to 4%, and the mixture was treated at 121 °C for 1 h to complete the dilute acid hydrolysis. After hydrolysis, the mixture was filtered and washed until the filtrate approached neutrality. The residue was dried at 105 °C to constant weight and weighed to obtain the acid-insoluble lignin (AIL). The collected filtrate was analyzed by UV-Vis spectrophotometer at around 240 nm to determine the acid-soluble lignin (ASL). The total lignin content of the sample was obtained by summing AIL and ASL. Accordingly, the lignin content of the CS used

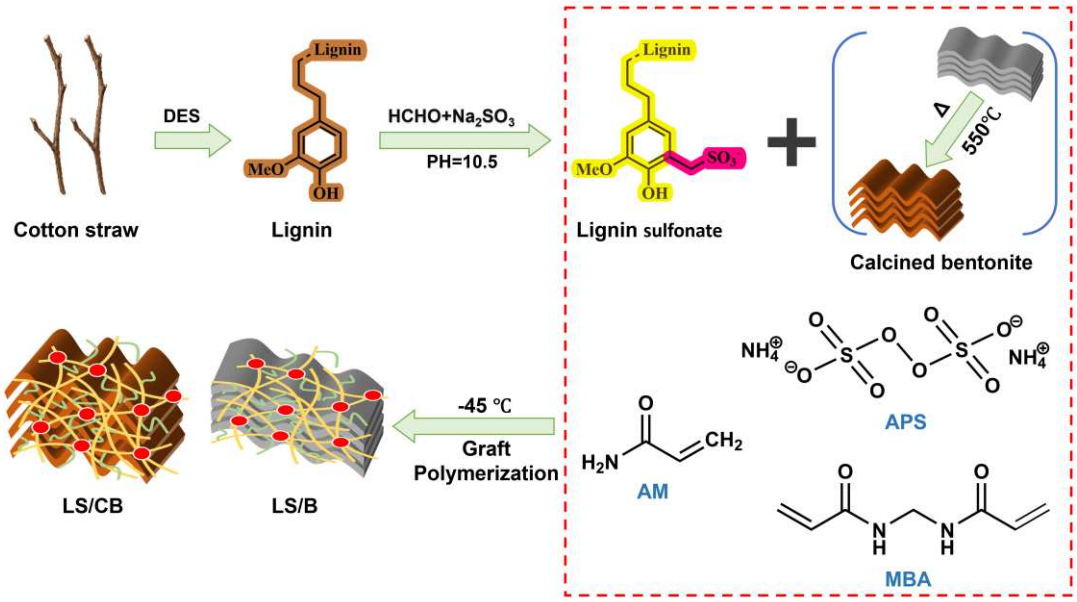
was determined to be 26.07%. The total lignin content was calculated according to Equation (1):

$$Y = \frac{m_{AIL}+m_{ASL}}{m_{sample}} \times 100\% \quad (1)$$

where m_{AIL} and m_{ASL} are the masses of acid-insoluble and acid-soluble lignin (g), respectively, and m_{sample} is the oven-dry weight of the raw material (g).

2.4 Fabrication of LS/CB and LS/B composites

To prepare LS, 0.5 g of lignin was dissolved in 15 mL of deionized water (pH adjusted to 10.5). Hydroxymethylation was conducted by dropwise addition of 0.35 mL of 37% HCHO solution at 75 °C for 2 h, followed by sulfonation with 0.2 g of Na_2SO_3 at 90 °C for 3 h. The reaction mixture was neutralized with hydrochloric acid and precipitated with 45 mL of anhydrous ethanol. The resulting precipitate was collected by centrifugation (8000 rpm, 10 min), washed, and vacuum-dried at 60 °C to obtain LS. Subsequently, to fabricate the composite hydrogels, 0.5 g of the SL aqueous solution was mixed with 0.5 g of bentonite (or CB) suspension. Then, 1 g of AM and 80 mg of MBA were added and stirred until completely dissolved, followed by the addition of 50 mg of APS. The mixture was sealed and reacted at 45 °C for 1 h. The resulting hydrogel was immersed in deionized water for 24 h to remove unreacted monomers and finally lyophilized at -45 °C to yield the LS/B and LS/CB composite hydrogels (Scheme. 1).



Scheme. 1. The synthesis routes for the LS/B and LS/CB composites.

2.5 Characterization

The functional groups of lignin, bentonite, and their composites were identified by Fourier transform infrared spectroscopy (FTIR, Bruker INVENIO R) over the wavenumber range of 500–4000 cm^{-1}. X-ray diffraction (XRD, Rigaku Smartlab, Japan) with Cu Kα radiation was employed to examine the crystal structures, scanning from 5° to 80° (2θ). Thermogravimetric analysis coupled with derivative thermogravimetry (TGA/DTG) was conducted at a heating rate of 10.0 °C/min under a nitrogen atmosphere, with the temperature ramped from 30 to 700 °C. The surface morphology of Au-sputtered samples was observed by high-resolution cold-field emission scanning electron microscopy (SEM) at an accelerating voltage of 5 kV. The molecular structure of DES-extracted lignin was further analyzed by two-dimensional heteronuclear single quantum coherence nuclear magnetic resonance (2D HSQC NMR, Bruker DMX-500, Germany, 600 MHz). X-ray photoelectron spectroscopy (XPS) was employed to probe the surface elemental composition and chemical states. Specific surface area was measured by nitrogen adsorption-desorption using a CIQTEK V-Sorb 2800TP analyzer.

2.6 Adsorption experiments and modeling

2.6.1 Batch adsorption experiments

Adsorption experiments followed a univariate approach. 150 mL MB solutions at initial concentrations from 50 to 400 mg·L^{-1} were equilibrated with 20-100 mg adsorbent in sealed flasks for 3 h at 150 rpm. Solution pH was adjusted between 2.0 and 10.0 prior to contact. For thermodynamic evaluation, runs were conducted at 298, 308, and 323 K. Aliquots were withdrawn at predetermined intervals up to 300 min, centrifuged at 8000 rpm for 8 min, and the residual MB concentration was determined at 664 nm. Equilibrium capacities q_e (mg·g^{-1}) and removal rate R (%) were calculated using. All determinations were performed in triplicate, and average values were used to compute q_e and R (%)via Equations (2) and (3), respectively:

$$q_e = \frac{(C_0 - C_e) \times V}{m} \tag{2}$$

$$R(\%) = \frac{C_0 - C_e}{C_0} \times 100 \tag{3}$$

where, C_0 and C_e denote the initial and equilibrium dye concentrations (mg·L^{-1}), respectively; V is the solution volume (L); and m represents the adsorbent mass (g).

2.6.2 Theoretical models

To elucidate the underlying sorption mechanisms, equilibrium data were analyzed using Langmuir and Freundlich isotherm models, while kinetic profiles were fitted with pseudo-first-order (PFO), pseudo-second-order (PSO), and intra-particle diffusion (IDM) models. Thermodynamic feasibility was evaluated via the van't Hoff equation. The mathematical expressions and corresponding parameter definitions are summarized in Table 1.

Table 1. Adsorption isotherm, kinetic, and thermodynamic models used in this study.

Category	Model	Equation
Isotherm	Langmuir	$\frac{1}{q_e} = \frac{1}{K_L q_{max} C_e} + \frac{1}{q_{max}}$
	Freundlich	$lnq_e = lnK_F + \left(\frac{1}{n}\right) lnC_e$
Kinetics	PFO	$ln(q_e - q_t) = lnq_e - k_1 t$
	PSO	$\frac{t}{q_t} = \frac{1}{k_2 {q_e}^2} + \frac{t}{q_e}$
	IDM	$q_t = K_{diff} t^{\frac{1}{2}} + C$
Thermodynamics	van't Hoff	$\Delta G^\circ = \Delta H^\circ - T\Delta S^\circ = -RTlnK_d$
		$K_d = \frac{q_e}{C_e}$
		$lnK_d = \frac{\Delta S^\circ}{R} - \frac{\Delta H^\circ}{RT}$

Note: q_{max}, maximum adsorption capacity (mg·g^{-1}); C_e, equilibrium concentration (mg·L^{-1}); K_L, Langmuir constant (L·mg^{-1}); K_F and $1/n$, Freundlich constants; q_t, adsorption capacity at time (mg·g^{-1}); k_1 and k_2, PFO (min^{-1}) and PSO (g·mg^{-1}·min^{-1}) rate constants; K_{diff}, intra-particle diffusion rate constant (mg·g^{-1}·min$^{-0.5}$); C, boundary layer thickness; K_d, distribution coefficient (L·mg^{-1}); R, gas constant (8.314 J·mol^{-1}·K^{-1}); T, absolute temperature (K); ΔG°, ΔH° and ΔS°, Gibbs free energy, enthalpy and entropy changes (kJ·mol^{-1}, kJ·mol^{-1}, and J·mol^{-1}·K^{-1}, respectively).

3 Results and Discussions

3.1 Lignin extraction and structural validation

Conventional alkaline extraction invariably cleaves phenolic –OH groups and oxidizes aromatic rings, damaging lignin's native structure. To preserve these critical features, DES extraction conditions were first investigated through single-factor experiments (Fig. 1) and subsequently subjected to systematic optimization, yielding a validated optimum of 130 °C, 8 h, ChCl:LA = 1:8, solid-to-liquid = 1:10, and 10 min ultrasonication. Under these conditions, the extraction achieved a yield of 82.90% with a relative deviation of merely 0.64% from the predicted value. The quadratic model demonstrated strong fit and predictive ability, as evidenced by R^2 = 0.9941 and predicted R^2 = 0.9890 (see Section 1.2 of the Supplementary Information).

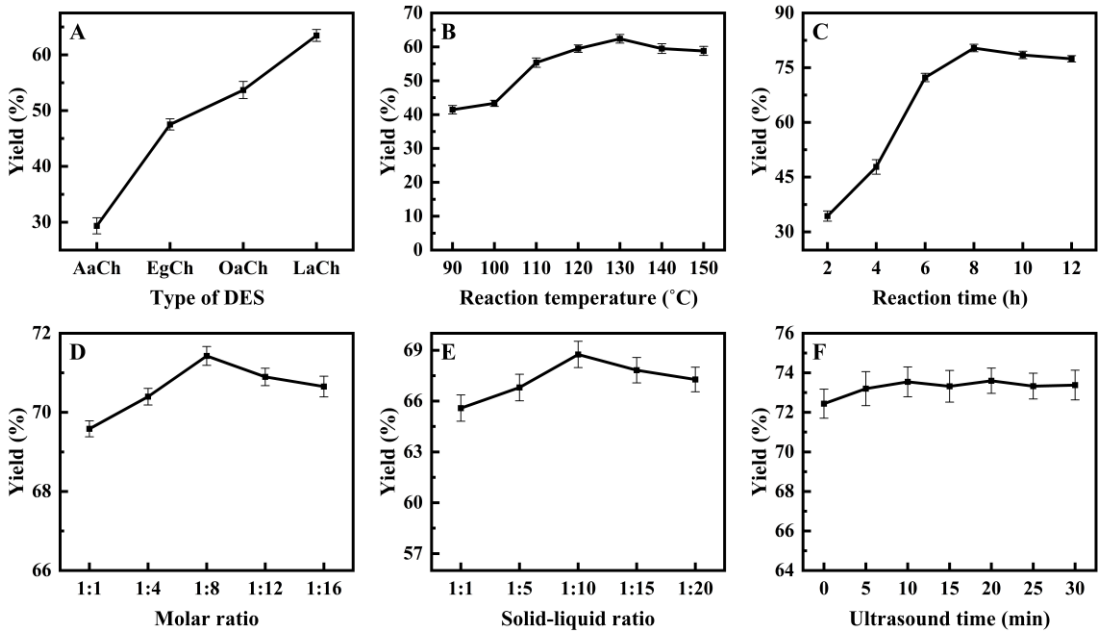


Fig. 1. Single-factor experiments for lignin pretreatment: Type of DES (A); Reaction temperature (B); Reaction time (C); Molar ratio (D); Solid-liquid ratio (E); Ultrasonic treatment time (F).

2D HSQC NMR confirmed the preservation of native lignin architecture. In the aliphatic side-chain region (Fig. 2A), β-O-4 aryl ether linkages dominated over β-5 and β-β substructures, with the characteristic Cγ–Hγ correlation at δC/δH 60.9/3.40 ppm, alongside prominent methoxyl signals at δC/δH 55.6/3.73 ppm [26]. The aromatic region (Fig 2B) distinctly revealed intact guaiacyl (G-type) units, evidenced by G_2 at δC/δH 110.8/7.01 ppm, G_5 at 115.0/6.67 ppm, and G_6 at 120.3/6.70 ppm [27]. The intact preservation of these β-O-4 linkages and G-rich aromatic platforms, abundant in phenolic –OH precursors and π-conjugated domains, directly furnishes high-density –SO_3H anchoring sites and π–π interaction loci upon subsequent sulfonation, constituting the fundamental structural origin of the adsorption performance demonstrated throughout this study.

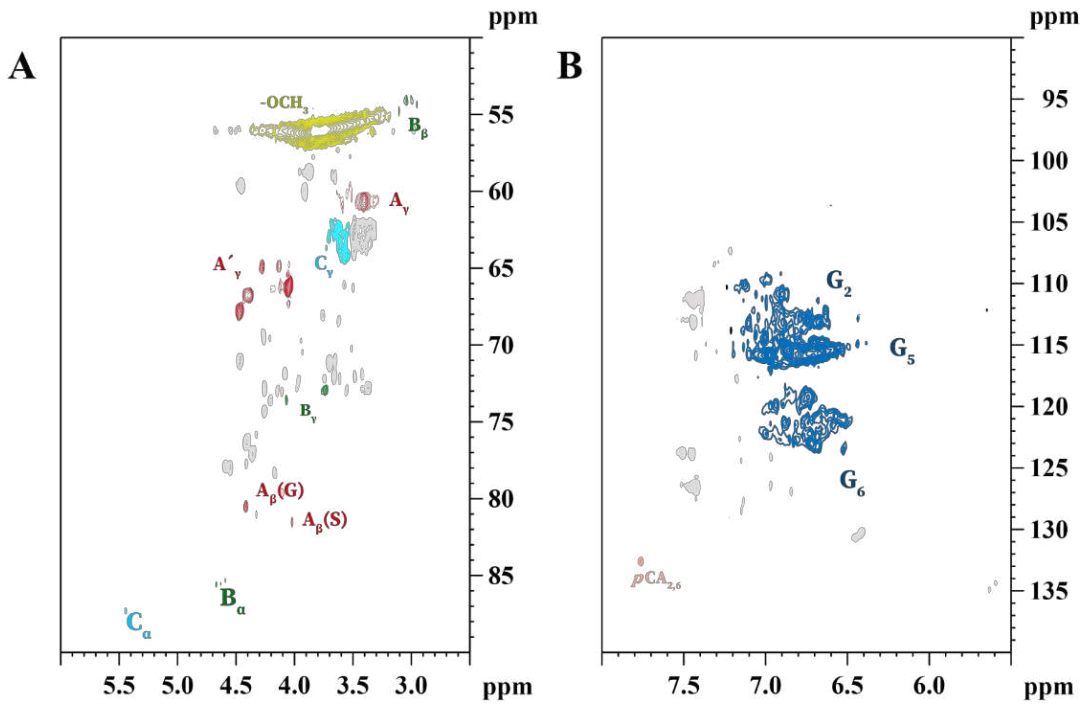


Fig. 2. Aliphatic side-chain region (A) and aromatic region (B) of the 2D HSQC NMR spectrum of lignin.

3.2 Structural design of composite hydrogels

To verify whether CB outperforms raw bentonite (B) in constructing an efficient adsorption network, the structural evolution from raw materials to composites was systematically traced. Thermogravimetric analysis showed that CB exhibited a mass loss of only 4.73% at 700 °C, compared with 7.55% for B, confirming effective impurity removal (Fig. 3A and B). XRD patterns further indicated that the characteristic peaks of B at 19.8°, 20.1°, and 26.6° were preserved in CB with markedly enhanced intensity, reflecting increased crystallinity [28] (Fig. 3C).

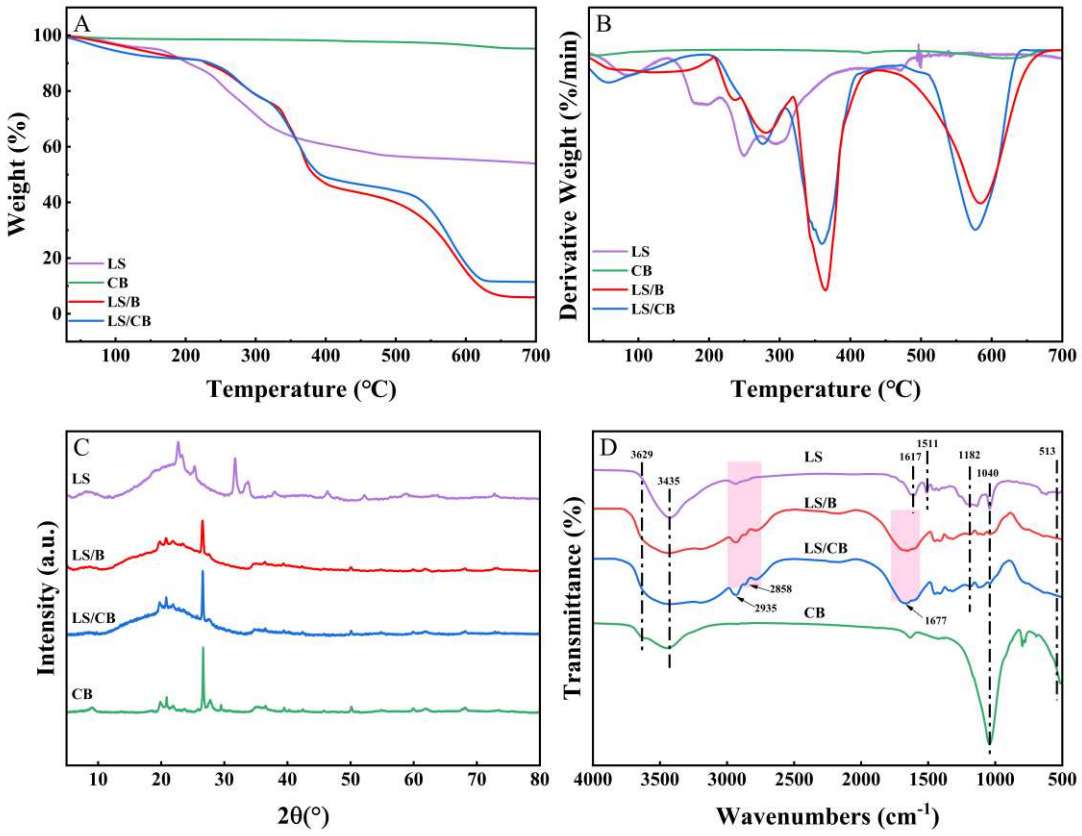


Fig. 3. TG and DTG curves of LS, bentonite, CB, LS/B and LS/CB (A) and (B); XRD spectra (C) and FT-IR spectra of LS, LS/B, LS/CB, CB and bentonite (D).

Sulfonation introduced sulfonate groups into lignin, as evidenced by S=O stretching vibrations at 1182 and 1040 cm^{-1} [29], and subsequent cross-linking integrated these components into a stable hydrogel network, reflected by the emergence of an amide C=O band at 1658 cm^{-1} and $–CH_2/–CH_3$ stretching vibrations at 2935 and 2858 cm^{-1} [30] (Fig. 3D). XPS spectra (Fig. 4C-E) further corroborated this architecture: the N 1s signal at 399.6 eV confirmed polyacrylamide-mediated hydrogen bonding between LS and bentonite, the S 2p peak at 168.1 eV verified retained sulfonate functionality [31], and the unshifted Si 2p peak at 102.1 eV demonstrated intact bentonite crystallinity.

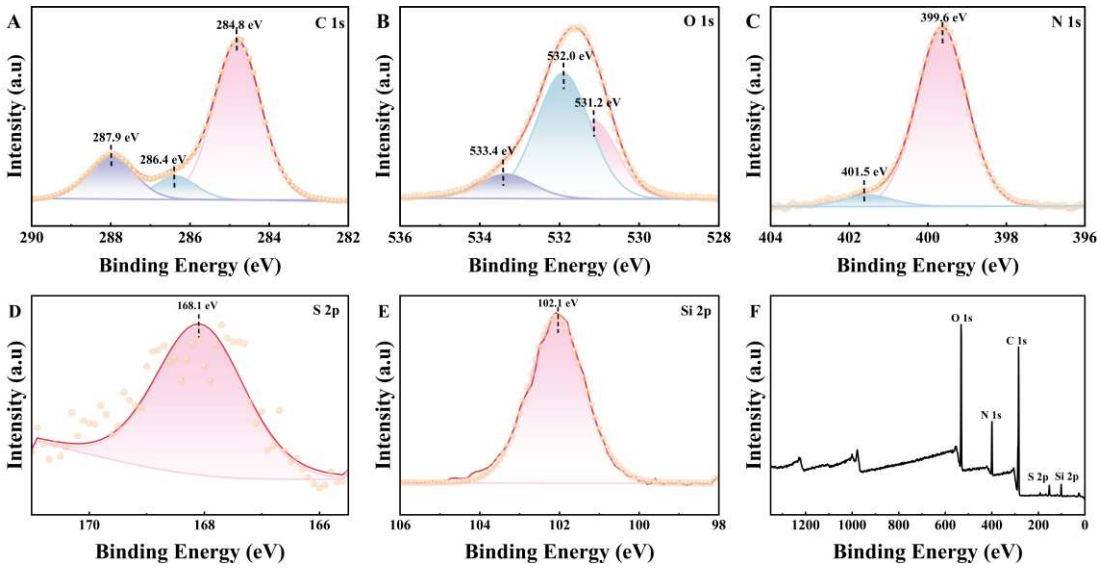


Fig. 4. XPS spectra of LS/CB: (A) C 1s; (B) O 1s; (C) N 1s; (D) S 2p; (E) Si 2p; and (F) LS/CB survey spectrum.

Morphologically, SEM (Fig. 5A and B) revealed a sharp contrast: LS/B possessed a loose structure with large, smooth pores, whereas LS/CB displayed a densely distributed mesoporous network with significantly reduced pore size and rougher walls. These densely packed small pores and the rough skeleton are expected to substantially increase the specific surface area, thereby providing more accessible contact sites for subsequent adsorption.

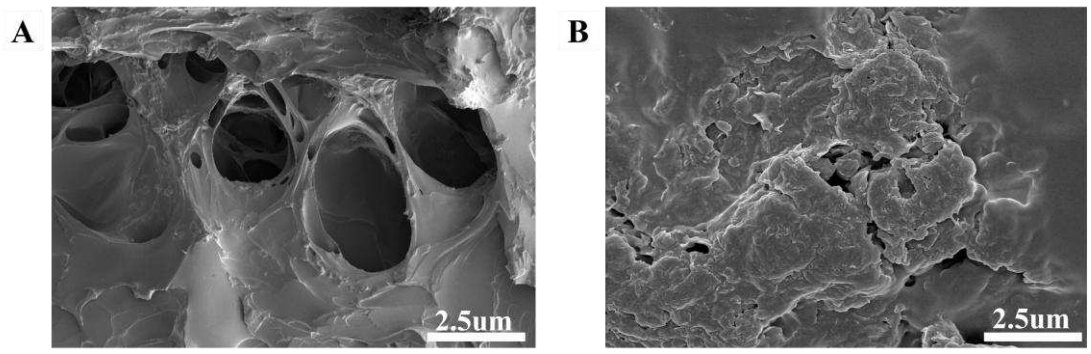


Fig. 5. SEM images of LS/B (A) and LS/CB (B).

Nitrogen sorption analysis (Fig. 6) quantitatively confirmed this structural transformation. The LS/CB hydrogel exhibited a Type IV isotherm with an H3

hysteresis loop, characteristic of slit-shaped mesopores concentrated in the 7-29 nm range, and a specific surface area of 52.64 $m^2 \cdot g^{-1}$. This dense mesoporous architecture furnishes abundant contact sites for adsorption while establishing the structural basis for the pore-diffusion behavior examined below.

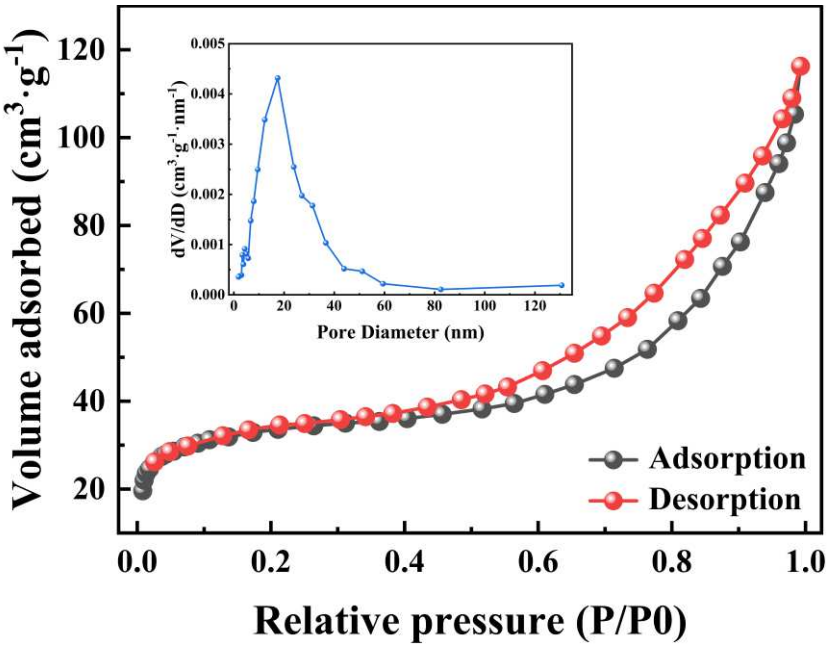


Fig. 6. BET curve of LS/CB.

3.3 Adsorption parameter dependence

Fig. 7 compares the adsorption behavior of LS/B and LS/CB under varying conditions. The optimal parameters were determined to be initial concentration 250 $mg \cdot L^{-1}$, adsorbent dosage 40 mg, contact time 120 min, pH 8.0, and temperature 308 K, this temperature was selected because further increasing to 323 K yielded only marginal capacity improvements for both hydrogels, as detailed in the thermodynamic analysis below. Under these conditions, LS/CB achieved a maximum capacity of 275.29 $mg \cdot g^{-1}$, consistently outperforming LS/B. Adsorption was strongly suppressed at pH 2.0 but increased sharply with deprotonation, peaking at pH 8.0 before a slight decline at pH 10.0.

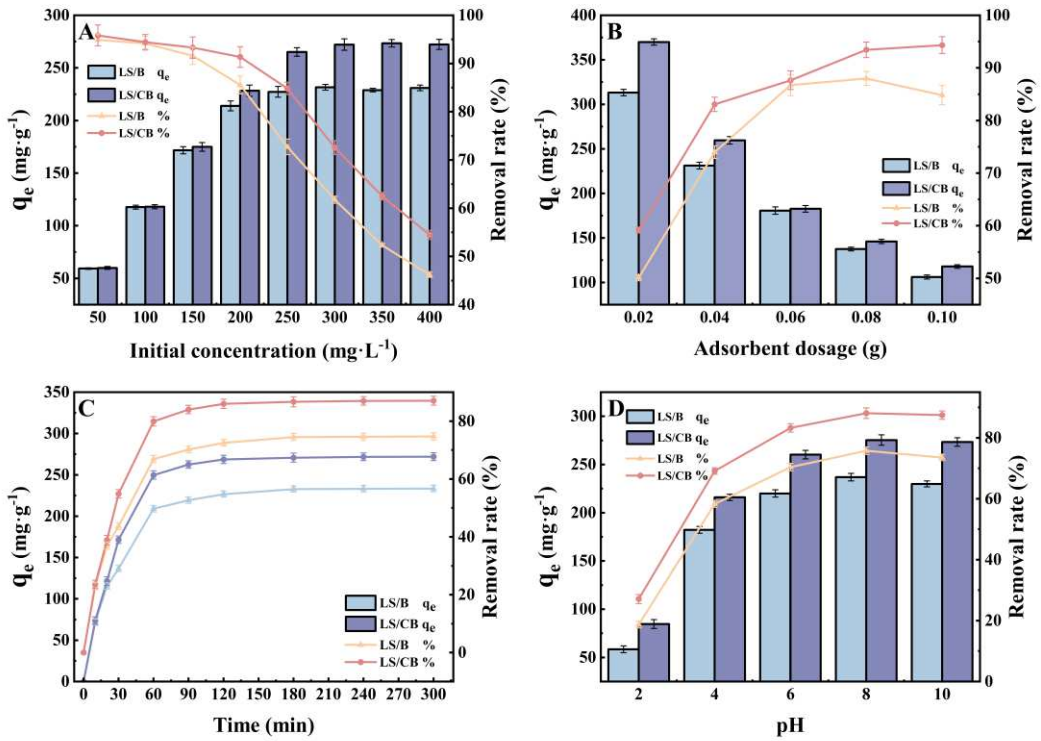


Fig. 7. Effect of initial concentration (A); adsorbent dosage (B); adsorption time (C); pH (D) on adsorption capacity and removal rate.

The superior performance of LS/CB stems from calcination-induced purification: raw bentonite contains exchangeable cations that compete with MB^+ under acidic conditions, whereas calcination removes these impurities and enhances structural rigidity. At pH 8.0, the sulfonate and silanol sites are fully deprotonated, maximizing ion-exchange efficiency, while the denser pore structure of LS/CB provides a higher density of accessible active sites per unit mass.

3.4 Adsorption isotherms, kinetics and thermodynamics

The fitting curves in Fig. 8 and the parameters listed in Table 2 show that the Langmuir model achieved R^2 values of 0.9970 for LS/B and 0.9931 for LS/CB, markedly higher than the Freundlich model. This confirms that both hydrogels follow a monolayer adsorption mechanism, structurally rooted in the high-density -SO_3H

anchoring sites and π–π interaction loci furnished by the intact β-O-4 linkages and G-rich aromatic platforms, as well as the fully deprotonated sulfonate and silanol sites at pH 8.0. The Langmuir maximum adsorption capacities were calculated as 252.53 mg·g^{-1} for LS/B and 293.26 mg·g^{-1} for LS/CB, values that closely match the experimental equilibrium capacities of 238.61 and 277.56 mg·g^{-1} respectively. The higher q_{max} of LS/CB reflects its calcination-induced purification and denser mesoporous network, which provides a higher density of accessible active sites per unit mass.

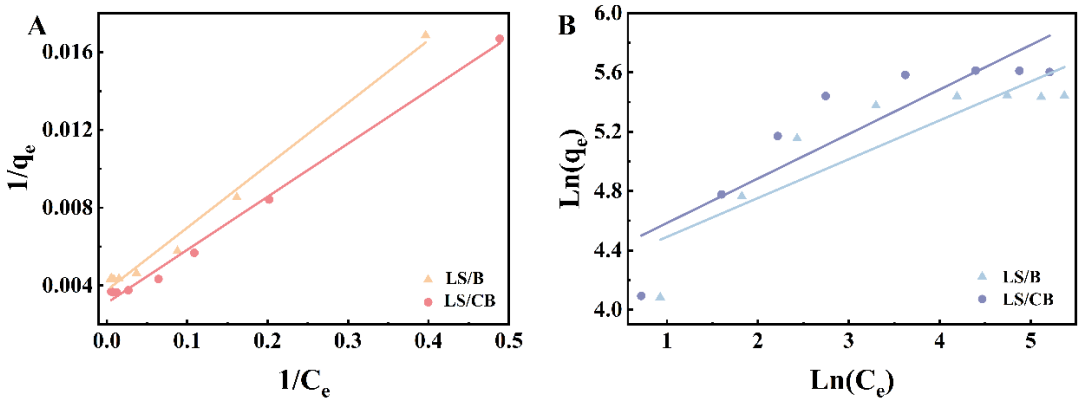


Fig. 8. Adsorption isotherm models: (A) Langmuir; (B) Freundlich.

Table 2. Parameters of Langmuir and Freundlich adsorption isotherm models.

Samples	Langmuir			Freundlich		
	q_m (mg·g^{-1})	K_L (L·mg^{-1})	R^2	K_F	1/n	R^2
LS/B	252.53	0.1235	0.9970	63.98	0.2619	0.7980
LS/CB	293.26	0.1237	0.9931	65.07	0.3000	0.8174

Table 3 compares the maximum MB adsorption capacity of the as-prepared adsorbent with those of related adsorbents previously reported in the literature. The LS/CB composite exhibits a maximum adsorption capacity of 277.56 mg·g^{-1}, which is higher than or comparable to most existing bentonite- or lignin-based adsorbents. This highlights the potential of the proposed modification strategy in enhancing the adsorption performance of bentonite- or lignin-based materials.

Table 3. Adsorption capacities of relevant adsorbents towards MB.

Adsorbent	Maximum adsorption capacity ($mg \cdot g^{-1}$)	Reference
CS-LIG aerogel	95.68	[32]
Lignin-PVA hydrogel	179	[33]
BC/Ca-MMT	338.8	[34]
CMC/ZnO/lignin hydrogel	276.79	[35]
PVP/PCMC/GO/bentonite hydrogel	172.14	[36]
Chitosan/lignin composite	74.07	[37]
Magnetic bentonite	86.20	[38]
L-SC@Fe_3O_4	281.4	[39]
Carrageenan-g-polyacrylamide/bentonite	156.25	[40]
LT/BC	151.20	[24]
LS/B	238.61	This work
LS/CB	277.56	This work

The kinetic data presented in Fig. 9A and B and summarized in Table 4 reveal that the PSO model achieves a markedly better fit than the PFO model for both hydrogels, and the equilibrium capacities predicted by this model are in close agreement with the experimental values. These findings demonstrate that chemisorption predominates for both materials, a behavior structurally underpinned by the sulfonate functionality and the polyacrylamide-mediated hydrogen bonding network stabilizing active sites within the hydrogel matrix.

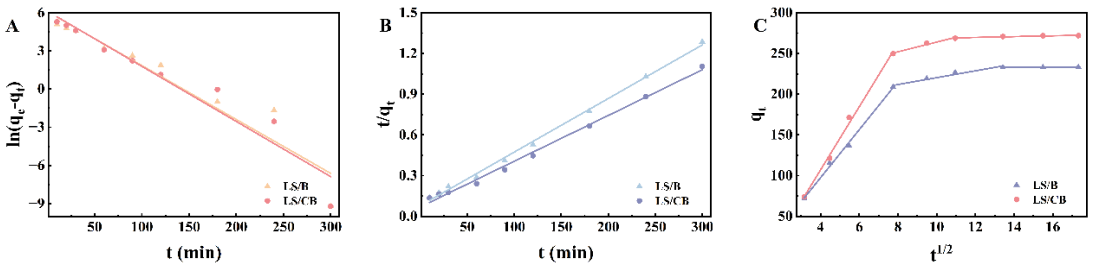


Fig.9. Adsorption kinetic models: (A) PFO; (B) PSO; (C) IDM.

Table 4. Parameters of PFO, PSO and IDM adsorption kinetic models.

Kinetic models	Kinetic parameters	Sample	
		LS/B	LS/CB
PFO	q_e (mg·g^{-1})	438.50	454.76
	k_1(min^{-1})	0.0423	0.0433
	R^2	0.9007	0.9222
PSO	q_e (mg·g^{-1})	253.16	296.74
	k_2 (g·mg^{-1}·min^{-1})	2.00×10^{-4}	1.66×10^{-4}
	R^2	0.9967	0.9939
IDM			
Step1	K_{p1}	29.50	38.79
	C_1	-20.58	-48.16
	R^2	0.9942	0.9936
Step2	K_{p2}	4.2036	5.9427
	C_2	178.21	204.51
	R^2	0.9355	0.9560
Step3	K_{p3}	0.0951	0.4950
	C_3	231.59	263.71
	R^2	0.9952	0.8141

The intra-particle diffusion plots in Fig. 9C and the parameters in Table 4 show that both hydrogels undergo three distinct diffusion stages with rate constants following the order $K_{p1} > K_{p2} > K_{p3}$. In the first stage, K_{p1} values of 29.50 and 38.79 correspond to rapid surface diffusion; the higher K_{p1} of LS/CB is consistent with its rougher surface morphology and larger specific surface area. In the second stage, the K_{p2} values decrease for both materials as the MB concentration drops and active sites become occupied, reflecting slower intra-particle diffusion through the mesoporous channels. In the third stage, K_{p3} values drop to 0.0951 and 0.4950 and the curves plateau, indicating equilibrium within the densely packed pore network. The consistently higher diffusion constants of LS/CB confirm that its densely packed mesoporous structure not only increases the active site density but also maintains more efficient mass transfer

channels even at the final equilibrium stage.

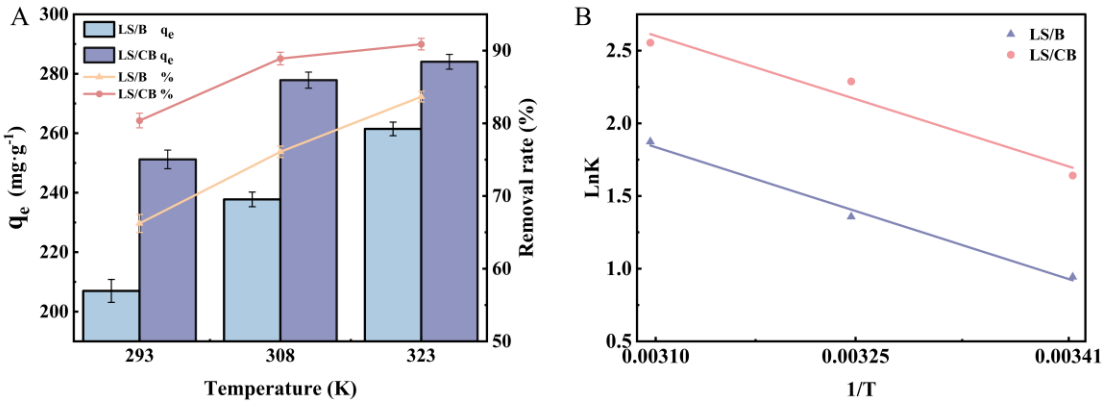


Fig. 10. Effect of LS/B and LS/CB at different temperatures adsorption capacity and removal rate(A); Adsorption thermodynamic model (B).

The temperature-dependent data in Fig. 10A show that both hydrogels exhibit increased adsorption capacity and removal efficiency with rising temperature. At 293 K, LS/B and LS/CB achieved capacities of 206.19 and 251.57 mg·g^{-1} with removal rate of 65.98% and 80.50%, respectively; at 323 K, these values rose to 261.16 mg·g^{-1} and 83.57% for LS/B, and 284.84 mg·g^{-1} and 91.14% for LS/CB. The van't Hoff plots in Fig. 10B and the thermodynamic parameters in Table 5 confirm positive $\Delta H°$ and negative $\Delta G°$ values for both materials, verifying an endothermic and spontaneous process that becomes more favorable at elevated temperatures.

Table 5. Parameters of adsorption thermodynamic models

Samples	T /K	ΔG /kJ·mol^{-1}	ΔH /kJ·mol^{-1}	ΔS /J·mol^{-1}·K^{-1}
LS/B	293	-2.30	24.34	90.72
	308	-3.48		
	323	-5.03		
LS/CB	293	-4.00	24.12	96.40
	308	-5.86		
	323	-6.86		

3.5 Reusability of materials

The adsorption-desorption cycle is a critical aspect of evaluating the practical applicability of an adsorbent. In this study, the regeneration process involved ultrasonic treatment in ethanol for 20 min, followed by washing with 0.1 $mol \cdot L^{-1}$ HCl and rinsing with deionized water until neutral. The dried hydrogels were then subjected to subsequent adsorption cycles. The removal efficiency and adsorption capacity in each cycle were used as indicators to assess the regeneration capability of the adsorbents.

As illustrated in Fig. 11, LS/CB exhibits superior recyclability, with its removal efficiency decreasing from 86.37% to 71.41% after five adsorption-desorption cycles, compared to a more pronounced drop for LS/B from 75.28% to 58.43%. This enhanced stability is likely stemming from the calcination treatment, which strengthens the bentonite framework and facilitates the preservation of active sites under acidic regeneration conditions [41].

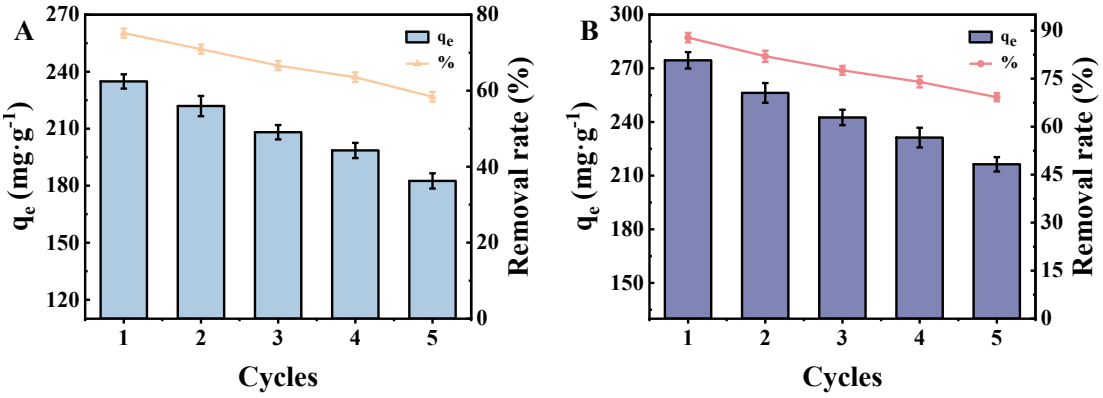


Fig. 11. Adsorption capacity and removal rate for five adsorption-desorption cycles:(A) LS/B; (B) LS/CB.

3.6 Mechanism insights

The adsorption mechanism of MB onto the hydrogel was investigated by integrating pH studies, isotherm, kinetic, and thermodynamic analyses with FTIR

characterization of LS/CB before and after adsorption. As shown in Fig. 12, the broad absorption band centered at 3425 cm^{-1} originates from the O-H stretching vibrations of phenolic and aliphatic hydroxyl groups in lignin. After MB adsorption, this band shifted to a higher wavenumber of ~3440 cm^{-1}, indicative of weakened hydrogen bonding and the deprotonation of phenolic hydroxyl groups on G-type lignin units, generating negatively charged phenolates ($-O^-$) [42,43]. These phenolate anions form electrostatic interactions with the cationic $N^+(CH_3)_2$ moieties of MB molecules, and this electrostatic adsorption mechanism is further confirmed by the simultaneous shift of phenolic C-O stretching vibration from ~1319 cm^{-1} to ~1392 cm^{-1}. The shift of the benzene ring C=C stretching vibration from 1458 cm^{-1} to 1498 cm^{-1} suggests the involvement of π-π stacking during the adsorption process. The variation in the sulfonic acid group peak at 1040 cm^{-1} provides additional evidence for the electrostatic adsorption mechanism.

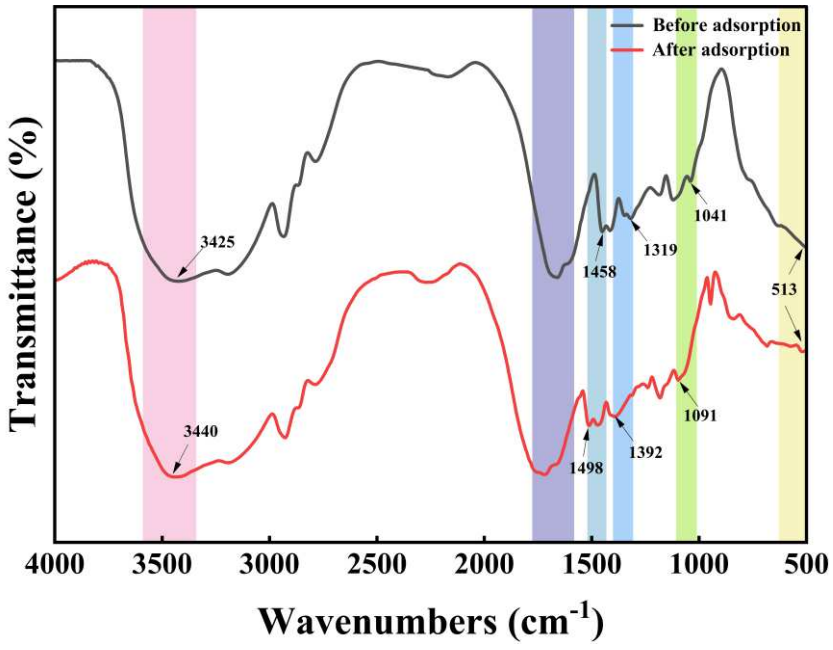


Fig. 12. FTIR spectra: LS/CB before and after MB adsorption.

In summary, the adsorption of MB onto LS/CB is primarily driven by electrostatic attraction, with π-π stacking and hydrogen bonding acting as synergistic auxiliary

mechanisms (Fig 13).

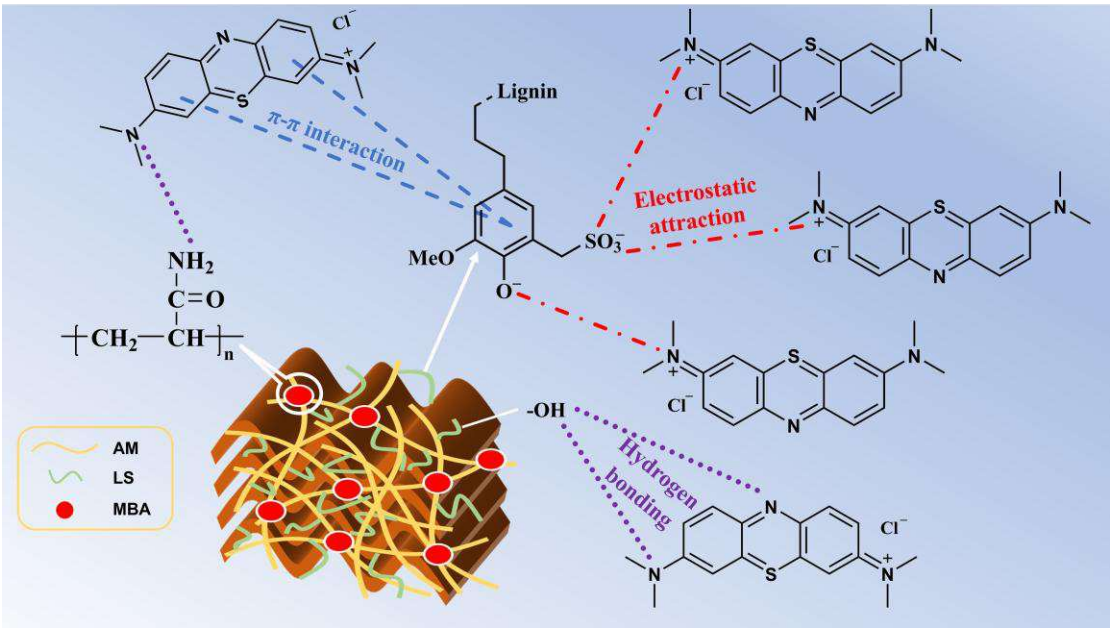


Fig. 13. Possible adsorption mechanisms between MB and LS/CB.

4 Conclusions

In this study, lignin was extracted from cotton straw using a lactic acid-based deep eutectic solvent (LA-DES), achieving an 82.90% yield under optimized conditions (130 °C, 8 h, ChCl:LA = 1:8, S/L = 1:10, 10 min ultrasonication). Characterization confirmed that the extracted lignin retained an intact aromatic backbone with a predominantly amorphous, guaiacyl-rich structure. The lignin was subsequently sulfonated and cross-linked with bentonite or CB to fabricate LS/B and LS/CB composite hydrogels with three-dimensional network structures. Under optimal conditions (250 $mg \cdot L^{-1}$ MB, 35 °C, 40 mg adsorbent, 2 h, pH 8), LS/CB exhibited a superior maximum adsorption capacity of 277.56 $mg \cdot g^{-1}$ compared to 238.61 $mg \cdot g^{-1}$ for LS/B. The adsorption followed Langmuir isotherm and pseudo-second-order kinetics, indicating spontaneous, endothermic, entropy-driven chemisorption primarily governed by electrostatic interactions, synergistically assisted by π–π stacking and

hydrogen bonding. After five regeneration cycles, LS/CB retained considerable removal efficiency, demonstrating superior cyclic stability. This work offers a sustainable strategy for converting agricultural waste into effective dye adsorbents.

CRediT authorship contribution statement

Nuermaimaiti Yimamu: Writing—original draft, Validation, Investigation, Visualization, Data curation, Formal analysis, Writing – review & editing. **Zheng Zheng Yao:** Validation, Investigation, Data curation, Conceptualization, Writing—original draft. **Xin Yu Wu:** Resources, Data curation. **Kai Ze Ding:** Resources, Data curation. **Tursunjan Aydan:** Review & editing, Supervision, Conceptualization, Methodology, Funding acquisition.

Declaration of competing interest

The authors declare that they have no known competing financial interests or personal relationships that could have appeared to influence the work reported in this paper.

Acknowledgments

This work was financially supported by the Natural Science Foundation of Xinjiang Uygur Autonomous Region (Grant No. 2022D01C29), China.

References

1. Cai C, Wang Z, Ma L, Xu Z, Yu J, Li F (2024) Cotton stalk valorization towards bio-based materials, chemicals, and biofuels: A review. Renewable and Sustainable Energy Reviews 202:114651.https://doi.org/10.1016/j.rser.2024.114651.

2. Tan F, Lu F, Yan Y, Wang Y, Wang X, Zhou J, Xu J (2026) Progress in preparation strategies for lignin-derived carbon aerogels and the regulation of their supercapacitor performance. Fuel 407:137371.https://doi.org/10.1016/j.fuel.2025.137371.

3. Wang B, Sun Y-C, Sun R-C (2019) Fractionational and structural characterization of lignin and its modification as biosorbents for efficient removal of chromium from wastewater: a review. Journal of Leather Science and Engineering 1 (1):1–25.https://doi.org/10.1186/s42825-019-0003-y.

4. Zhang Z, Chen Y, Wang D, Yu D, Wu C (2023) Lignin-based adsorbents for heavy metals. Industrial Crops and Products

193:116119.https://doi.org/10.1016/j.indcrop.2022.116119.
5. Zhang H, Xue K, Wang B, Ren W, Sun D, Shao C, Sun R (2024) Advances in lignin-based biosorbents for sustainable wastewater treatment. Bioresource Technology 395:130347.https://doi.org/10.1016/j.biortech.2024.130347.
6. Dandash AA, Jdayil BA, Tannous JH (2025) Lignin Extraction from Various Biomass Sources: A Comprehensive Review of Characteristics, Applications, and Future Prospects. Chemical record (New York, NY) 25 (8):e2500045.https://doi.org/10.1002/tcr.202500045.
7. Sun S-C, Sun S-F, Xu Y, Wen J-L, Yuan T-Q (2023) Green and sustainable production of high-purity lignin microparticles with well-preserved substructure and enhanced anti-UV/oxidant activity using peroxide-promoted alkaline deep eutectic solvent. International Journal of Biological Macromolecules 253:127057.https://doi.org/10.1016/j.ijbiomac.2023.127057.
8. Liu X, Wei W, Wu S (2019) Synergism of organic acid and deep eutectic solvents pretreatment for the co-production of oligosaccharides and enhancing enzymatic saccharification. Bioresource Technology 290:121775.https://doi.org/10.1016/j.biortech.2019.121775.
9. Rodrigues JS, de Freitas AdSM, Maciel CC, Mendes SF, Diment D, Balakshin M, Botaro VR (2023) Selection of kraft lignin fractions as a partial substitute for phenol in synthesis of phenolic resins: Structure-property correlation. Industrial Crops and Products 191:115948.https://doi.org/10.1016/j.indcrop.2022.115948.
10. Wang X, Zhang Y, Jia S, Deng H, Xu W, Shi J (2024) Unraveling lignin's structural features for catalytic oxidative depolymerization and enhanced renewable resource utilization. Industrial Crops and Products 207:117750.https://doi.org/10.1016/j.indcrop.2023.117750.
11. Jiang P, Peng B, Han Y, Li G, Ikkala O, Chu F (2024) Colloidal lignin valorization: From macromolecular design to targeted applications. Progress in Polymer Science 154:101839.https://doi.org/10.1016/j.progpolymsci.2024.101839.
12. Mengqi S, Shoujuan W, Yuebin X, Weijun Y, Xuliang L, Xueqing Q, Fengshan Z, Fangong K (2025) Preparation of chemically modified lignin and its application in advanced functional materials. Resources Chemicals and Materials 4 (3):100104.https://doi.org/10.1016/j.recm.2025.100104.
13. Wang T, Jiang M, Yu X, Niu N, Chen L (2022) Application of lignin adsorbent in wastewater Treatment: A review. Separation and Purification Technology 302:122116.https://doi.org/10.1016/j.seppur.2022.122116.
14. Diksha K, Bhavanam A, Giribabu D (2025) Lignin and black liquor based composite hydrogels for the enhanced adsorption of malachite green dye from aqueous solutions: Kinetics, rheology and isotherm studies. International Journal of Biological Macromolecules 296:139613.https://doi.org/10.1016/j.ijbiomac.2025.139613.
15. Bhuiyan RH, Rahman MM, Billah MM, Ehsan MF, Akter T, Hossain MS, Rashid MM, Islam MS, Ray SK (2026) Bio-adsorbent for wastewater treatment: amination of green coconut husk waste-derived lignin for the removal of Congo red dye. RSC Advances 16 (3):2093–2111.https://doi.org/10.1039/d5ra07573d.
16. Kubra MJ, Ahmed T, Rahaman MS, Hasnine SMM, Sultana S, Mortuza F, Sultana N, Alam MA (2025) Eco-friendly Lignin/N,N-dimethylacrylamide Hydrogel with Carrageenan and Polyvinylpyrrolidone for Amphoteric Adsorption of Methylene Blue and Congo Red: Optimization, Characterization, and Adsorption. International Journal of Biological Macromolecules 306:141471.https://doi.org/10.1016/j.ijbiomac.2025.141471.
17. Barrios N, Marquez R, Trovagunta R, Tolosa L, Suarez A, Zambrano F,

Gonzalez R, Pal L, Hubbe MA (2025) Lignin self-assembly phenomena and valorization strategies for pulping, biorefining, and materials development: Part 2. Factors affecting the specificity of lignin self-assembly for industrial applications. Advances in Colloid and Interface Science 342:103521.https://doi.org/10.1016/j.cis.2025.103521.

18. Morales A, Labidi J, Gullón P (2022) Influence of lignin modifications on physically crosslinked lignin hydrogels for drug delivery applications. Sustainable Materials and Technologies 33:e00474.https://doi.org/10.1016/j.susmat.2022.e00474.

19. Sharma N, Yadav A, Yadav S, Panghal P, Singh S, Deep A, Kumar S (2024) Biomass-based adsorbents for wastewater remediation: A systematic review on removal of emerging contaminants. Microchemical Journal 207:111880.https://doi.org/10.1016/j.microc.2024.111880.

20. Gandhi D, Bandyopadhyay R, Soni B (2022) Naturally occurring bentonite clay: Structural augmentation, characterization and application as catalyst. Materials Today: Proceedings 57:194–201.https://doi.org/10.1016/j.matpr.2022.02.346.

21. Arabmofrad S, Lazzara G, Miller R, Jafari SM (2024) Surface modification of bentonite and montmorillonite as novel nano-adsorbents for the removal of phenols, heavy metals and drug residues. Advances in Colloid and Interface Science 334:103334.https://doi.org/10.1016/j.cis.2024.103334.

22. Fu X, Cao L, Zhang S, Meng S, Yang Y, Li YC, Liu G, Tong Z (2024) A sustainable lignin-clay nano-absorbent for highly efficient methylene blue removal. International Journal of Biological Macromolecules 282:137030.https://doi.org/10.1016/j.ijbiomac.2024.137030.

23. Fang Y, Qiu Y, Xi Y, Si L, Wang W, Peng W, Cao Y (2026) Amino-functionalized montmorillonite/lignin hybrid hydrogel for efficient Pb(II) capture through synergistic ion exchange and coordination. Journal of Environmental Chemical Engineering 14 (5):123692.https://doi.org/10.1016/j.jece.2026.123692.

24. Yao Z, Yimamu N, Wu X, Ding K, Aydan T (2026) A cotton straw-based modified lignin-bentonite composite for efficient adsorption of methylene blue dye. Surfaces and Interfaces 94:109485–109485.https://doi.org/10.1016/j.Surfin.2026.109485.

25. B SJ, O RR, J SC, D SA, W TD (2010) Compositional analysis of lignocellulosic feedstocks. 1. Review and description of methods. Journal of agricultural and food chemistry 58 (16):9043–9053.https://doi.org/10.1021/jf1008023.

26. Jorge R, Ana G, Lidia N, J J-B, B FC, Hoon K, John R, T MA, C DRJ (2011) Lignin composition and structure in young versus adult Eucalyptus globulus plants. Plant physiology 155 (2):667–682.https://doi.org/10.1104/pp.110.167254.

27. Sun R-C, Wen J-L, Xue B-L, Sun S-L (2013) Recent Advances in Characterization of Lignin Polymer by Solution-State Nuclear Magnetic Resonance (NMR) Methodology. Materials 6 (1):359–391.https://doi.org/10.3390/ma6010359.

28. Tadesse SH (2022) Application of Ethiopian bentonite for water treatment containing zinc. Emerging Contaminants 8:113–122.https://doi.org/10.1016/j.emcon.2022.02.002.

29. Kamoun A, Jelidi A, Chaabouni M (2003) Evaluation of the performance of sulfonated esparto grass lignin as a plasticizer–water reducer for cement. Cement and Concrete Research 33 (7):995–1003.https://doi.org/10.1016/S0008-8846(02)01098-0.

30. Ramesan MT, Surya K (2016) Synthesis, characterization, and properties of cashew gum graft poly(acrylamide)/magnetite nanocomposites. Journal of Applied Polymer Science 133 (22):n/a–n/a.https://doi.org/10.1002/app.43496.

31. Sun S-F, Wan H-F, Zhao X, Gao C, Xiao L-P, Sun R-C (2023) Facile

construction of lignin-based network composite hydrogel for efficient adsorption of methylene blue from wastewater. International Journal of Biological Macromolecules 253:126688.https://doi.org/10.1016/j.ijbiomac.2023.126688.

32. Zhu Y, Qi BK, Lv HN, Gao Y, Zha SH, An RY, Zhao QS, Zhao B (2023) Preparation of DES lignin-chitosan aerogel and its adsorption performance for dyes, catechin and epicatechin. Int J Biol Macromol 247:125761.https://doi.org/10.1016/j.ijbiomac.2023.125761.

33. Wu L, Huang S, Zheng J, Qiu Z, Lin X, Qin Y (2019) Synthesis and characterization of biomass lignin-based PVA super-absorbent hydrogel. Int J Biol Macromol 140:538–545.https://doi.org/10.1016/j.ijbiomac.2019.08.142.

34. Hu Y, Chen C, Yang L, Cui J, Hao Q, Sun D (2019) Handy purifier based on bacterial cellulose and Ca-montmorillonite composites for efficient removal of dyes and antibiotics. Carbohydr Polym 222:115017.https://doi.org/10.1016/j.carbpol.2019.115017.

35. Fu J, Yap JX, Leo CP, Chang CK (2024) Enhanced photocatalytic regeneration of carboxymethyl cellulose/lignin/ZnO complex hydrogel after methylene blue adsorption. Int J Biol Macromol 274 (Pt 2):133510.https://doi.org/10.1016/j.ijbiomac.2024.133510.

36. Dai H, Huang Y, Huang H (2018) Eco-friendly polyvinyl alcohol/carboxymethyl cellulose hydrogels reinforced with graphene oxide and bentonite for enhanced adsorption of methylene blue. Carbohydrate Polymers 185:1–11.https://doi.org/10.1016/j.carbpol.2017.12.073.

37. Sohni S, Hashim R, Nidaullah H, Lamaming J, Sulaiman O (2019) Chitosan/nano-lignin based composite as a new sorbent for enhanced removal of dye pollution from aqueous solutions. International Journal of Biological Macromolecules 132:1304–1317.https://doi.org/10.1016/j.ijbiomac.2019.03.151.

38. Chaabna I, Delimi R, Testas R (2024) Removal of methylene blue using magnetic Na-bentonite composite in aqueous Solutions. Desalination and Water Treatment 318.https://doi.org/10.1016/j.dwt.2024.100353.

39. Dai K, Zhao G, Kou J, Wang Z, Zhang J, Wu J, Yang P, Li M, Tang C, Zhuang W, Ying H (2021) Magnetic mesoporous sodium citrate modified lignin for improved adsorption of calcium ions and methylene blue from aqueous solution. Journal of Environmental Chemical Engineering 9 (2).https://doi.org/10.1016/j.jece.2021.105180.

40. Pourjavadi A, Bassampour Z, Ghasemzadeh H, Nazari M, Zolghadr L, Hosseini SH (2016) Porous Carrageenan-g-polyacrylamide/bentonite superabsorbent composites: swelling and dye adsorption behavior. Journal of Polymer Research 23 (3).https://doi.org/10.1007/s10965-016-0955-z.

41. Fode TA, Jande YAC, Kivevele T (2024) Effects of raw and different calcined bentonite on durability and mechanical properties of cement composite material. Case Studies in Construction Materials 20:e03012–.https://doi.org/10.1016/j.Cscm.2024.E03012.

42. Zhu Y, Ying L, Du X, Guo L, Zhu G, Lu H (2025) Revealing the mechanism underlying the phase transitions of high-amylose maize starch in ethylene glycol: An experimental and molecular dynamics simulation study. Food Chemistry: X 28:102597–102597.https://doi.org/10.1016/j.Fochx.2025.102597.

43. Tkachenko O, Diment D, Rigo D, Stromme M, Budnyak TM (2024) Unveiling the Nature of lignin's Interaction with Molecules: A Mechanistic Understanding of Adsorption of Methylene Blue Dye. Biomacromolecules 25 (7):4292–4304.https://doi.org/10.1021/acs.biomac.4c00371.

Supplementary Files

This is a list of supplementary files associated with this preprint. Click to download.

- SupplementaryInformation.docx